Full-Scale Application of Porous Leading-Edge Treatments in a Fan Stage for Mitigating Rotor-Stator Interaction Noise

Teruna, C.; Rego, Leandro; Casalino, D.; Ragni, D.; Avallone, F.

DOI
10.2514/6.2022-2963

Publication date
2022

Document Version
Final published version

Published in
28th AIAA/CEAS Aeroacoustics 2022 Conference

Citation (APA)
Teruna, C., Rego, L., Casalino, D., Ragni, D., & Avallone, F. (2022). Full-Scale Application of Porous Leading-Edge Treatments in a Fan Stage for Mitigating Rotor-Stator Interaction Noise. In *28th AIAA/CEAS Aeroacoustics 2022 Conference* Article AIAA 2022-2963 (28th AIAA/CEAS Aeroacoustics Conference, 2022). https://doi.org/10.2514/6.2022-2963

Aeroacoustics Conferences
June 14-17, 2022, Southampton, UK
28th AIAA/CEAS Aeroacoustics 2022 Conference

10.2514/6.2022-2963

Full-Scale Application of Porous Leading-Edge Treatments in a Fan Stage for Mitigating Rotor-Stator Interaction Noise

Christopher Teruna [*], Leandro Rego [†], Damiano Casalino [‡], Daniele Ragni [§], Francesco Avallone [¶]

High-fidelity numerical simulations have been performed to investigate the noise reduction capability of porous leading-edge treatments for mitigating rotor-stator interaction noise in a full-scale aircraft model. The aircraft model consists of the NASA High-Lift Common Research Model (HL-CRM) airframe combined with an up-scaled Source Diagnostic Test (CRM) fan stage. The leading edge of the fan-stage stator blades is made of porous serrations, modelled using the properties of a metal foam. It is found that the porous serrations induce flow separation at the suction side of the stator blades, especially in the inner span regions. As a result, the modified fan stage produces smaller thrust, and the broadband noise emission in the low-frequency range is enhanced. Nevertheless, the tonal noise components at the blade-passage frequency and its harmonics are mitigated by up to 6 dB. By limiting the usage of porosity near the tip of the stator blade, the adverse aerodynamic effects can be mitigated, improving the overall benefit of the porous serrations. Compared to the baseline case, such treatment leads to a total sound power level reduction 1.5 dB and a thrust penalty that is below 1.5 %. Hence, this study suggests that the aerodynamic effects of a porous leading-edge treatment should not be neglected in the design phase in order to maximise the noise reduction benefits.

I. Nomenclature

Λ = serration wavelength
μ = dynamic viscosity
∇p = pressure gradient
ϕ = porosity
A, = cross-section area of the fan stage
BPF_1, = blade-passage frequency
c, = chord length of the baseline OGV
C , $\boldsymbol{C}$, = form coefficient (tensor)
$C_{p,\mathrm{mean}}$ = mean surface pressure coefficient
$C_{p,\mathrm{rms}}$ = root-mean-square of surface pressure fluctuations
d_p = mean pore size
EPNL = effective perceived noise level
H = serration amplitude
K, $\boldsymbol{K}$, = permeability (tensor)
L_x, L_z = turbulence length scale in the axial (x) and radial (z) directions
$\dot{m}$ = mass flow rate
PWL = source power level with reference pressure 1×10^{-12} W
$\boldsymbol{R}_V$ = viscous resistivity
$\boldsymbol{R}_I$ = inertial resistivity
SPL = sound pressure level with reference pressure 20 µPa
U_{ref} = reference velocity based on average fan tip speed
$||\boldsymbol{U}||$ = mean velocity magnitude
$||\boldsymbol{U}_{\mathrm{RMS}}||$ = root-mean-square of the fluctuations of velocity magnitude

---

[*] Doctoral candidate, Wind Energy Department, Delft University of Technology, Delft 2629HS, The Netherlands. AIAA Student Member.
[†] Doctoral candidate, Wind Energy Department, Delft University of Technology, Delft 2629HS, The Netherlands. AIAA Student Member.
[‡] Professor, Wind Energy Department, Delft University of Technology, Delft 2629HS, The Netherlands. AIAA Member.
[§] Associate professor, Delft University of Technology, Delft 2629HS, The Netherlands. Wind Energy Department, AIAA Member.
[¶] Assistant professor, Wind Energy Department, Delft University of Technology, Delft 2629HS, The Netherlands. AIAA Member.

II. Introduction

Aircraft noise reduction has become an important objective already in the design phase of new airliners as regulations surrounding airborne noise pollution are becoming more stringent. Many airliners today are powered by high-bypass ratio turbofan, in which the fan stage components have been identified as major sources of noise. One of the most significant noise generation mechanisms is the impingement of the turbulent fan wake on the outlet-guide vanes (OGVs) [1]. In the past decades, the reduction of fan-stage noise emission has been achieved by realising cut-off modes by selecting a particular number of OGVs and fan blades, and by employing passive noise control method, such as acoustic liner. Nevertheless, as the bypass ratio of turbofans is expected to increase to reduce fuel consumption, the space available for acoustic liner is also likely to decrease due to the shortened axial length of the nacelle and the larger diameter of the engine. Because of the shorter axial length, the OGVs will be closer to the fan blades. As a consequence, the turbulent fan wake impinging on the OGVs will contain stronger and more coherent turbulent structures. Therefore, the unsteady loading induced on the OGV becomes more intense, leading to a stronger noise emission. For this reason, a novel noise mitigation technique might be required to pursue a quieter aircraft configuration.

The fan wake-OGV interaction mechanism can be considered as a case of turbulence-impingement noise generation mechanism [2], for which several leading-edge (LE) modifications have been suggested as noise mitigation technologies, such as serrations and porous materials. The former is a modification of the LE shape along the blade span with the aim to reduce the coherence of the noise scattering phenomena at different spanwise positions [3]. Recent studies have shown that the noise reduction level of sinusoidal serrations can be maximised by choosing certain wavelength Λ (spanwise tip-to-tip distance) and amplitude H (tip-to-root distance), such that $\Lambda/L_z \approx 4$ and $H/L_x \leq 2$ [4, 5], where L is the integral turbulence length scale in the streamwise (x) and spanwise (z) directions respectively. In contrast to serrations, the usage of porous leading edge allows for mitigating the distortion of impinging vortical structures by allowing them to permeate into the porous medium [6]. It has been shown that the noise reduction level tends to be higher as the permeability of the leading edge is increased [7, 8] although this also comes at the cost of reduced aerodynamic performance. Nevertheless, there has been no conclusive approach for optimising the porous LE design to the authors' best knowledge. In fact, novel permeable LE designs are still being actively investigated at the time of writing [8–11].

The usage of permeable treatment has been considered promising by several authors, but it is worth mentioning that many of these investigations were performed using simplified, laboratory-scale models, which cannot completely replicate the physical environment of a full-scale system. This can be partly attributed to the cost of studying a full-scale configuration, but such investigation can be considered crucial for assessing the efficacy of noise mitigation solutions, particularly during the initial design phase. More recently, aeroacoustic investigations of a full-scale aircraft configuration have become possible with the combination of parallel computing and high-fidelity numerical methods [12, 13]. By employing a similar approach, the present study investigates the application of porous serrations on the OGVs of a fan stage of an aircraft model. This investigation will provide insights into the effects of the implementation of such noise mitigation technologies on both acoustics and aerodynamics performances.

The remainder of this manuscript is structured in the following order. Section III provides an overview of the lattice-Boltzmann solver that has been employed, followed by the description of the simulation setup in section IV. Simulations results are discussed in section V. The manuscript is concluded with section VI.

III. Numerical Technique

The commercial software 3DS Simulia PowerFLOW 6-2019 based on lattice-Boltzmann (LB) method is used. The software solves the discrete Boltzmann equation for a finite number of directions. The LB method determines the macroscopic flow variables starting from the mesoscopic kinetic equation. The discretization used for this particular application consists of 19 discrete velocities in three dimensions (D3Q19), involving a third-order truncation of the Chapman-Enskog expansion [14]. The particle distribution function is solved on a Cartesian mesh, known as a lattice. An explicit time integration and a collision model are used, where the formulation based on a unique Galilean invariant is employed. The equilibrium distribution of Maxwell-Boltzmann is adopted [14].

A very-large eddy simulation (VLES) model is implemented to take into account the effect of the sub-grid unresolved scales of turbulence. Following Yakhot and Orszag [15], a two-equations $k - \epsilon$ Renormalization Group is used to compute a turbulent relaxation time that is added to the viscous relaxation time. To reduce computational cost, a wall model is used to approximate the no-slip boundary condition on solid walls; it is based on the extension of generalized law-of-the-wall model that takes into account the effect of pressure gradient. These equations are solved iteratively from the first cell close to the wall in order to specify the boundary conditions of the turbulence model. For this purpose, a

	NASA HL-CRM	Airbus A330-300
Fuselage length (m)	62.8	63.6
Wing span (m)	58.7	60.3

	NASA SDT (5.5:1 scale)	Rolls-Royce Trent 1000
Fan diameter (m)	2.93	2.85
Bypass ratio	-	10.8 - 11.0
Fan blade count	22	20
OGV blade count	26	46

Table 1 Comparisons between the NASA-CRM/SDT geometries against some real-life examples.

slip algorithm, obtained as generalization of a bounce-back and specular reflection process, is used.

Far-field noise is computed using the Ffowcs-Williams and Hawkings (FW-H) analogy [16]. A forward-time solution [17] of the FW-H equation based on Farrasat's formulation 1A [18], that is extended for the application on a permeable surface, has been employed.

The porous medium region has been modelled as an equivalent fluid region. The flow permeating this region will be subjected to a momentum loss following the Darcy's law, which states that the pressure gradient ∇p for a flow permeating through a porous material is proportional to the local flow velocity $\boldsymbol{u}$, as follows:

$$\nabla p = -\boldsymbol{R} \cdot \boldsymbol{u} \tag{1}$$

where $\boldsymbol{R}$ is the total resistivity which represents the sum of the viscous and inertial resistivity components ($\boldsymbol{R}_V$ and $\boldsymbol{R}_I$ respectively). Eq. 1 is also referred to as Darcy's force equation. $\boldsymbol{R}$ can be expanded as in Eq. 2, where the viscous and inertial resistivity can be related to the permeability $\boldsymbol{K}$ and form coefficient of the porous material respectively $\boldsymbol{C}$.

$$\boldsymbol{R} = \boldsymbol{R}_V + \boldsymbol{R}_I \boldsymbol{u} \ ; \qquad \boldsymbol{R}_V = \frac{\mu}{\rho \boldsymbol{K}} \ , \ \boldsymbol{R}_I = \boldsymbol{C} \tag{2}$$

At the interface between the porous medium region and that of regular fluid, double-sided surfaces are applied similar to sliding mesh [19]. Moreover, to satisfy mass-flux conservation at the interface, the following expression is adopted;

$$|\rho u_n|_\infty = \phi |\rho u_n|_{\mathrm{PM}} \tag{3}$$

where ϕ is the material porosity, while the subscripts ∞ and PM denote the regular fluid region and porous media region respectively.

IV. Simulation Setup

A full-scale aircraft model has been obtained by combining two geometries, both of which were developed by NASA. The airframe (i.e., fuselage and lifting surfaces) is based on the High-Lift Common Research Model (HL-CRM) geometry, which resembles a typical transonic wide-body airliner. Although the CRM model has flow-through (empty) nacelles, in this study the fan stage model from the Source Diagnostic Test (SDT) rig has been added. The aircraft configuration is shown in Fig. 1. The SDT fan stage is up-scaled by 11:2 in order match the dimension of a similar high-bypass ratio turbofan, as indicated in table 1. Due to this, the up-scaled fan operates at a lower rotational speed (i.e., 1420 RPM) than that in the original SDT study [20] in order to maintain the same fan tip speed $U_{\mathrm{ref}} = 237.57\,\mathrm{m/s}$. Up-scaling is not needed for the CRM geometry as it was already made available in full scale.

To mitigate the fan wake-OGV interaction noise in the fan stage, porous serrations has been used to modify the OGV LE. This solution has been chosen based on authors' previous investigation on a rod-airfoil configuration [9], where the serration planform has been found to be highly effective for addressing the tonal noise component, and the

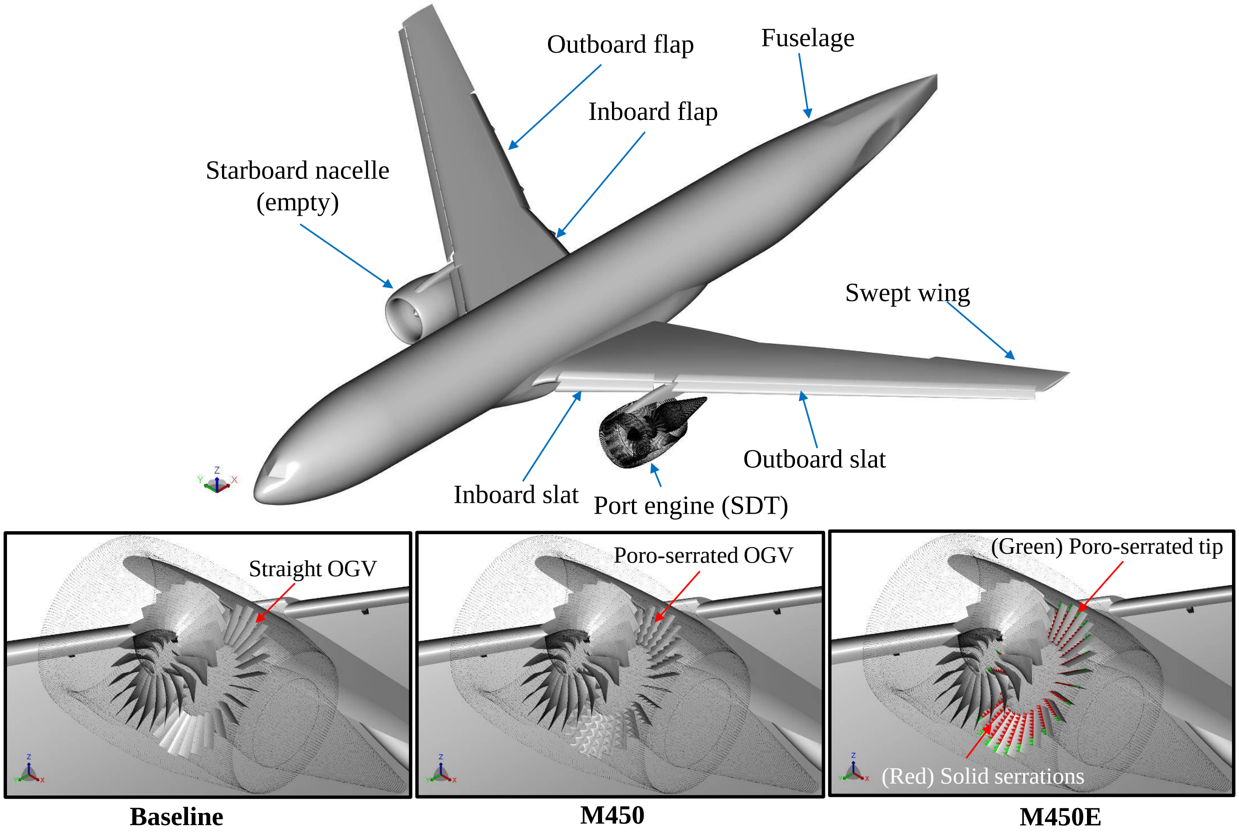

Fig. 1 The NASA HL-CRM/SDT configuration in the present study. The lower part of the figures shows a comparison between the baseline configuration the modified ones with poro-serrated OGVs.

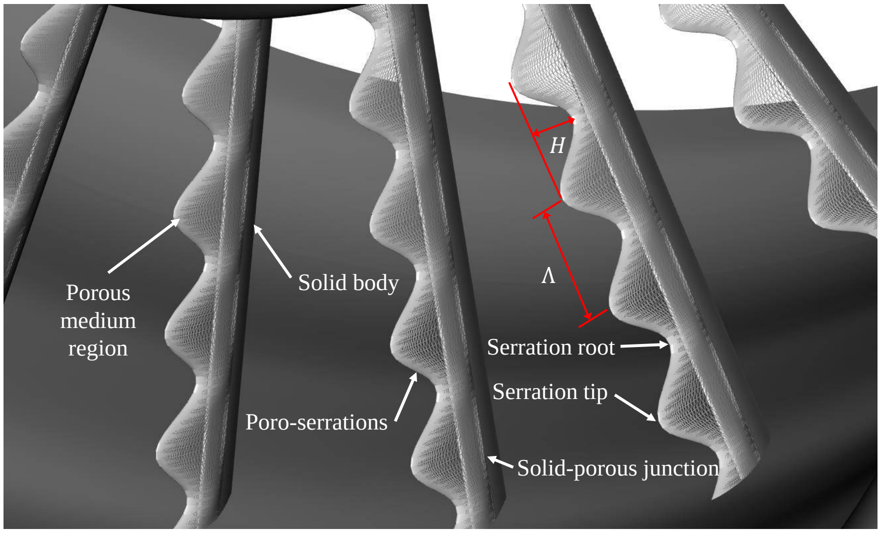

Fig. 2 A closer view of the M450 OGV in the fan stage, highlighting the amplitude H and wavelength Λ of the serration planform.

Type	d_p (µm)	ϕ(%)	K (m^2)	C (m^{-1})
Metal foam (M450/M450E)	450	89.28	6.11×10^{-10}	9758

Table 2 The properties of porous materials employed for the poro-serrated OGVs.

surface porosity for the broadband one. A closer view of the poro-serrated OGV in the fan stage is provided in Fig. 2. The porous serrations are implemented in the simulations as an equivalent fluid region where the properties of a Ni-Cr-Al metal foam with a mean pore diameter of 0.45 mm [21] have been imposed. The properties of the metal foam are reported in table 2. The serration planform is characterized by a wavelength $\Lambda = 0.76c$ and amplitude $H = 0.38c$, where $c = 218.5$ mm is the average chord length of the OGV. While the serration planform effectively modifies the first 20 % of the OGV chord, the porous medium region extends further downstream up to 60 % of the OGV chord, wrapping around a solid core. As it will be shown in the next subsection, the serration parameters have been optimised based on the turbulence length scales upstream of the OGV. To distinguish the modified OGV from the baseline one, the former will be referred to as the M450 configuration. In addition to the M450 configuration, another porous serrations design has been considered, which is referred to as the M450E configuration. In this case, the porous medium region is applied only at the outer 85 % of the OGV radius as noise sources at these locations are expected to be the strongest [22]. In other words, the serrations along the inner span of the OGV are fully solid (impermeable). Furthermore, the serration wavelength in the M450E configuration is half of that of the M450, whereas the amplitude remains the same.

Fig. 3 shows a cubic simulation domain whose sides are 1400 m long, or roughly 24 times the aircraft wingspan, and the CRM/SDT model is located at the center. All domain boundaries are specified as "inlets" with a freestream velocity of 68 m/s and a static pressure of 101 325 Pa, although PowerFLOW allows inlet boundaries to behave as outlets when required by the numerical solution. The aircraft is installed at an incidence of 7 deg to mimic the descending flight path during the approach phase. The figure also shows the permeable surface that encloses the port nacelle for the computation of far-field noise using FW-H acoustic analogy. 6 end-caps are added at the downstream end of the permeable surface to filter pseudo-sound contamination from the jet plume. The permeable surface samples pressure and velocity fluctuations at 5.93 kHz, which corresponds to a Nyquist frequency that equals to 5.7 times the blade-passage frequency ($\mathrm{BPF}_1 \approx 520$ Hz). Data are sampled for 1.32 s, which is roughly equivalent to 31 fan rotational cycles. An acoustic sponge region has been specified starting from a radius of 258 m (i.e., 4 times the length of the CRM fuselage) from the aircraft's nose to prevent acoustic reflection at the domain boundaries.

There are a total of 16 grid refinement regions, where the grid resolution level varies by a factor of 2 between adjacent regions. The finest grid resolution level is located inside the fan stage and at regions surrounding the jet plume, where the voxel size is equal to 2.54 mm or 0.0116c. This is equivalent to 33 grid points along the axial distance between the serration tip and root. The simulation is carried out for a total of 2.56 s with an initial transient of 1.24 s.

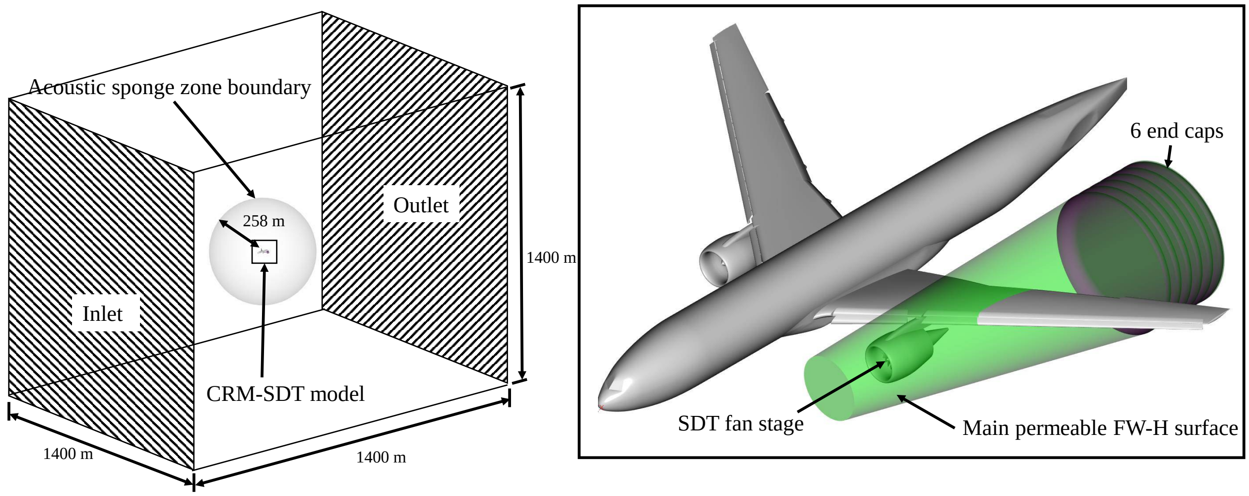

Fig. 3 (Left) The simulation domain enclosing the CRM/SDT model. (Right) The permeable FW-H surface for far-field noise analyses.

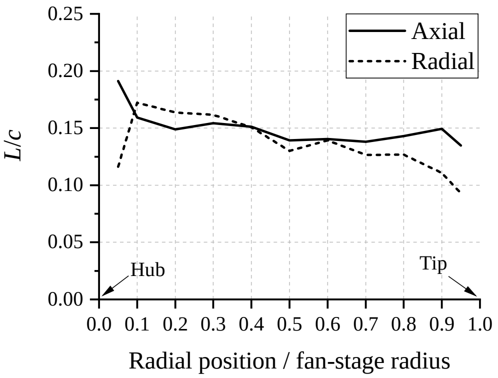

Fig. 4 The axial and radial integral length scales of turbulence in the interstage for the baseline configuration.

The simulations have been carried out using the Dutch National Supercomputer facility (Cartesius) with 720 cores of Intel-Haswell Xeon E5-2690 v3. The computational cost is approximately 95 000 CPU hours for the M450 configuration (i.e., the case with full-span poro-serrated OGVs).

V. Results

A. Integral length scales and serration design verification

Obtaining the integral length scales in the fan wake is essential for optimising the serration design. At present, the integral length scales are computed at axial locations halfway in between the fan and OGV blades, which will be referred to as the interstage in subsequent sections. The procedure mimics that in Podboy et al. [23] where axial and radial velocity fluctuations are measured locally using a hotwire probe. The integral length scales are then calculated by invoking the Taylor's frozen turbulence hypothesis as follows:

$$L_i = \langle \boldsymbol{U} \rangle \int_0^\infty \frac{\langle u_i(t) u_i(t+\Delta t) \rangle}{u_i^2} \mathrm{d}t \tag{4}$$

where $\boldsymbol{U}$ is the local velocity magnitude, u_i is the velocity fluctuations in the i^{th} direction, and $\langle \cdot \rangle$ is an ensemble averaging operator.

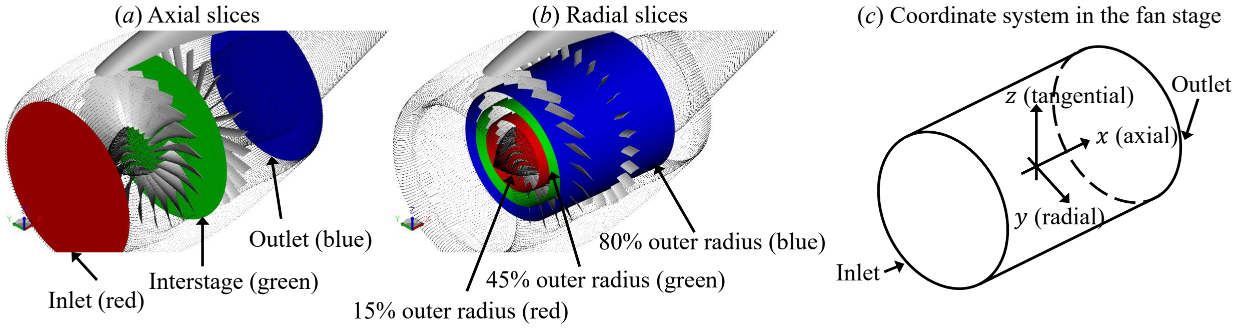
(*a*) Axial slices

(*b*) Radial slices

(*c*) Coordinate system in the fan stage

Fig. 5 A sketch of the slice planes where contours are plotted on in the subsequent figures. The cylindrical coordinate system in the fan stage is described in (*c*).

The variation of axial and radial length scales along the fan-stage radius for the baseline configuration is shown in Fig. 4. In the axial direction, the integral length scale is around $L_x = 0.15c$, although it can reach up to $0.19c$ near the hub. Regardless, the usage of a serration amplitude $H = 0.38c$ still satisfy the optimal ratio $H/L_x \leq 2$. The radial length scale (L_z) tends to decrease towards the outer fan-stage radius, varying in between $0.17c$ and $0.1c$. The serration wavelength in the M450 configurations is $\Lambda = 0.76c$, which satisfies the optimal ratio $\Lambda/L_z \approx 4$ near the hub, but overestimates near the tip. In order to maximise noise attenuation at the outer radius of the OGV where local noise sources are expected to be the strongest, the serrations in the M450E are designed using a shorter wavelength of $\Lambda = 0.38c$.

B. Flow statistics and fan-stage thrust

Flow statistics will be showns at different locations as indicated in Fig. 5. Figure (*a*) shows 3 axial slices at the fan-stage inlet, the interstage between the fan blades and the OGVs, and the fan-stage outlet. Aside from the axial slices, radial slices are also shown at 10 %, 45 %, and 80 % of the outer radius of the fan stage, as shown in (*b*).

Phase-locked statistics are presented as they allow capturing the periodic flow phenomena at each fan blade passage. Firstly. the phase-locked mean velocity magnitude contours ($||\boldsymbol{U}||$) along the different axial positions are shown in Fig. 6. The $||\boldsymbol{U}||$ values have been non-dimensionalized with the average fan tip speed $U_{\text{ref}} = 237.57$ m/s. Due to the incidence angle between the fan stage and the incoming flow, the flow distribution at the fan-stage inlet is not uniform, such that the velocity at the lower side of the fan stage is higher than at the upper side. The velocity magnitude for the M450 configuration is slightly lower than for the M450E and the baseline cases, indicating that the mass flow rate at the inlet decreases due to the poro-serrated OGVs. The contours at the interstage exhibit spiral patterns due to the swirl induced by the fan rotation. These patterns do not appear to be affected by the presence of the poro-serrated OGVs. A noticeable discrepancy in the velocity magnitude is evident at the fan-stage outlet. $||\boldsymbol{U}||$ near the hub is significantly lower in the M450 case. The reduction in mean velocity magnitude is less severe for the M450E configuration due to the limited spanwise extent of porous LE treatment. It is clear that the usage of porous serrations decreases the flow throughput in the fan stage, thus resulting in lower thrust.

The fan-stage thrust has been computed using the following equation:

$$\text{Thrust} = \left(\dot{m}_{\text{outlet}} U_{x,\text{outlet}} - \dot{m}_{\text{inlet}} U_{x,\text{inlet}}\right) + \left(p_{\text{outlet}} - p_{\text{inlet}}\right) A_{\text{outlet}} \tag{5}$$

where $\dot{m}$ is the mass-flow rate, U_x is the mean axial velocity, p is the local static pressure, and A is the cross-section area of the fan stage. Using this equation, the thrust produced by the baseline configuration is found to be 70.64 kN. The M450 configuration causes a thrust penalty of 7.5 %, which corresponds to a thrust of 64.22 kN. The thrust reduction for the M450E configuration is milder and of 1.4 %, which evidences that shortening the porous treatment is beneficial for the aerodynamic performance [7].

The mean velocity magnitude contours on the radial slices are shown in Fig. 7. The slice at 10 % of the outer radius reports a minor flow separation near the OGV trailing edge for the baseline case. Flow separation becomes more severe in the M450 case, whereas the solid serrations behave more closely to the baseline one. As a consequence, the average mean velocity in the fan-stage cross section downstream of the M450 OGVs becomes lower with respect to the

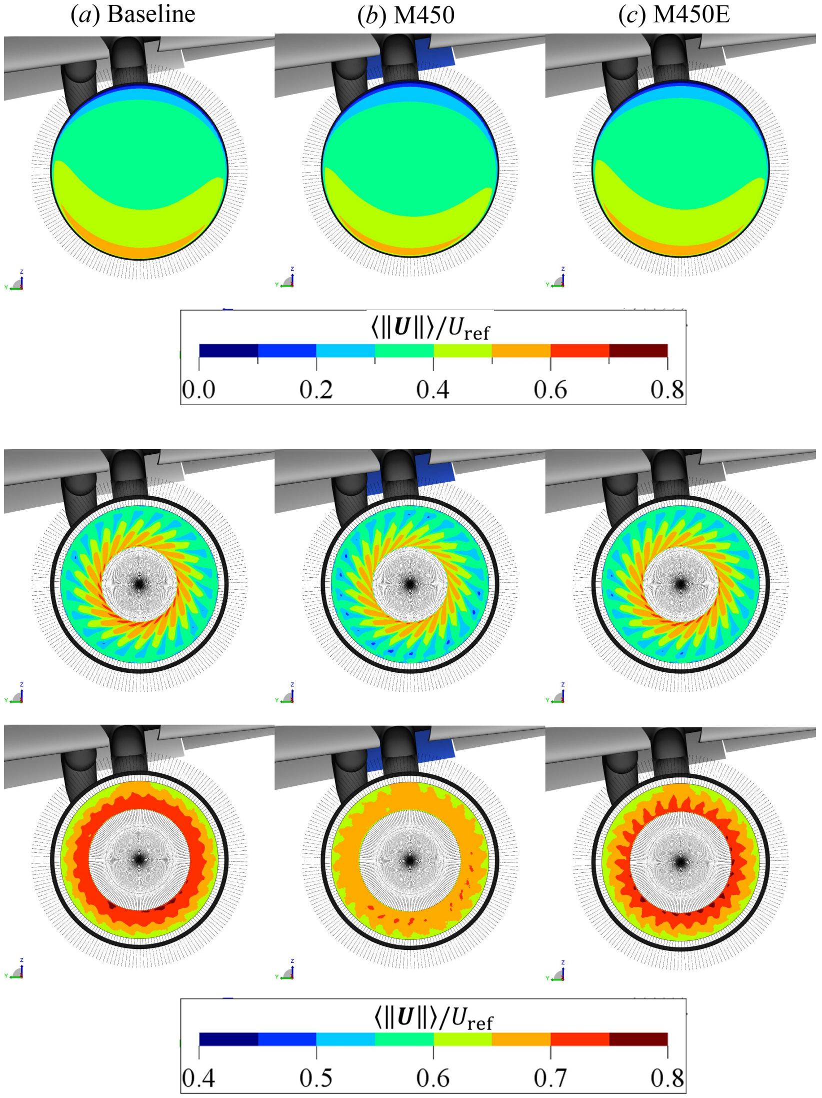

Fig. 6 (Front view) Contours of phase-locked average of velocity magnitude ($||U||$) at the SDT inlet (top row), interstage (middle row), and outlet (bottom row).

baseline one, which is responsible for the lower thrust described earlier. The flow separation is induced by the cross flow through the porous medium that is driven by pressure imbalance between the suction and pressure sides of the OGV. Such pressure balancing process also leads to a reduced efficacy of swirl recovery in the M450 configuration, which is evidenced by the steeper wake trail downstream of the OGV compared to that in the baseline case. This is particularly noticeable in the slices at 45 % of the outer radius. The contours at the lowermost row are plotted at 80 % of the outer radius, where the flow behavior in the three cases is more similar, hence supporting the design of the M450E configuration where porosity is implemented only at the outer span of the OGV.

The unsteady velocity field in the fan stage is examined in Fig. 8 and 9. They show the RMS (i.e., standard deviation) of velocity magnitude $||\boldsymbol{U}_{\mathrm{RMS}}||$. In the former, the swirl patterns can be clearly identified in the interstage. The intensity of velocity fluctuations increases further away from the hub; therefore, it is expected that the fan-wake impingement at the outer span of the OGV would yield to stronger noise. The axial contours at the fan-stage outlet clearly show that the poro-serrated OGVs in the M450 case strongly enhance the velocity fluctuations downstream of them because of the flow separation. The same phenomena are depicted by the radial slices in Fig. 9. Interestingly, the $||\boldsymbol{U}_{\mathrm{RMS}}||$ levels in the wake of the M450E OGVs appear to be slightly weaker than in the baseline case. This might be due to the generation of streamwise vortices, starting from the serration tip [24, 25], which help re-energising the boundary layer at the suction

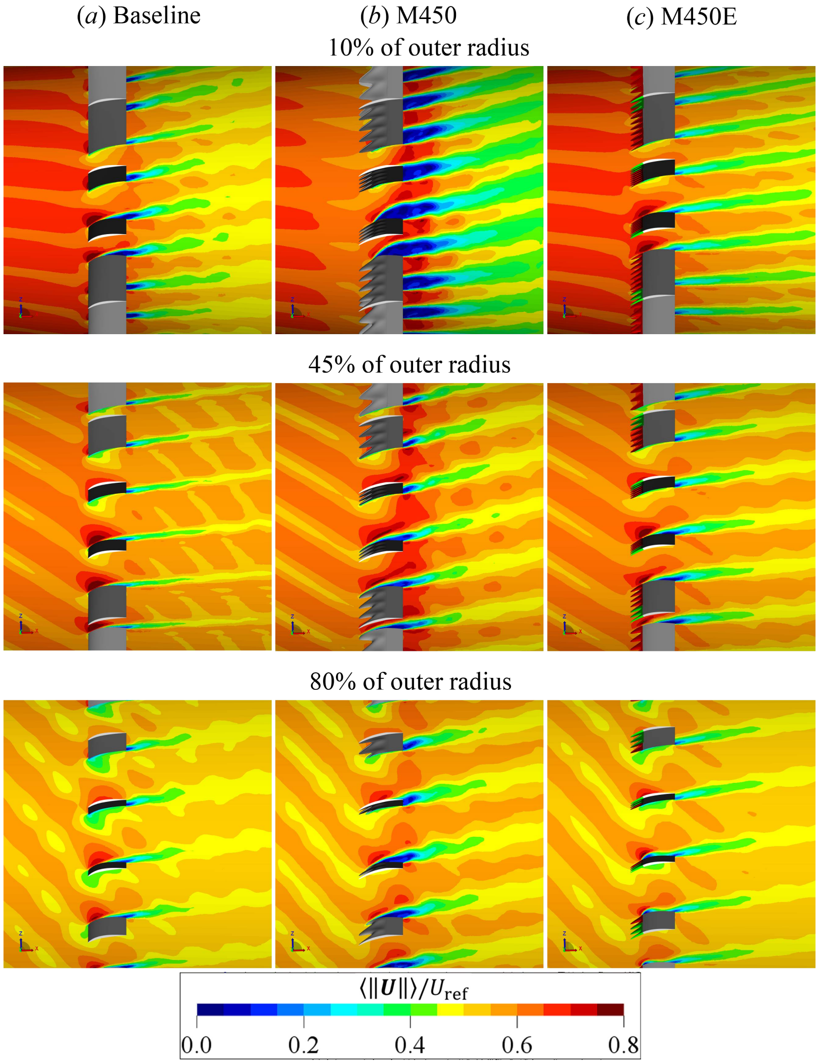

Fig. 7 (Side view) Contours of phase-locked average of velocity magnitude $||U||$ at the different radial sections (top - 10 %, middle - 45 %, and bottom - 80 % of the outer radius) in the fan stage.

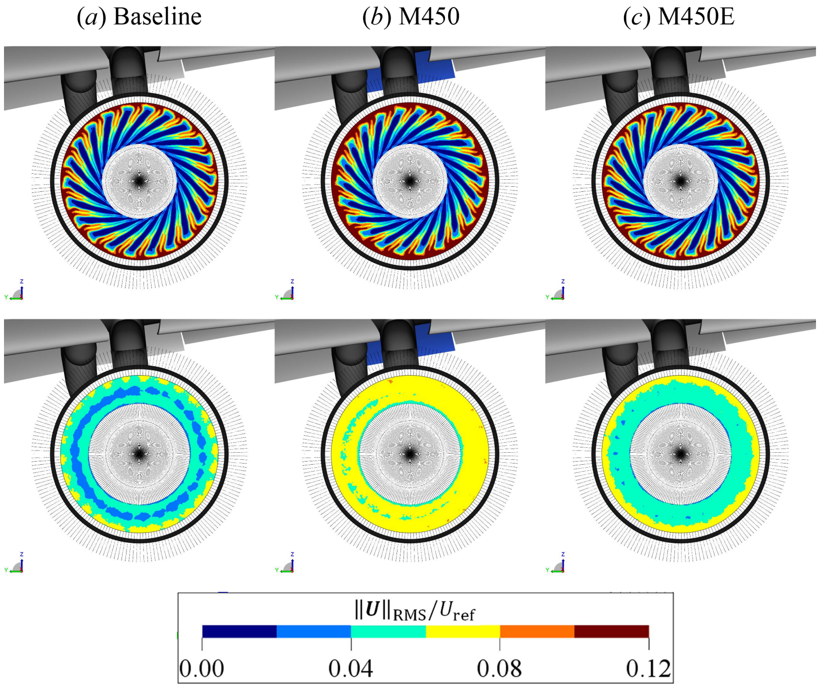
(*a*) Baseline (*b*) M450 (*c*) M450E

Fig. 8 (Front view) Contours of phase-locked standard deviation of velocity magnitude ($||U_{\mathrm{RMS}}||$) at the SDT interstage (top row) and outlet (bottom row).

side of the OGV. At other radial positions, the influence of the separated-flow regions in the M450 configuration can still be observed, although it becomes less severe further away from the hub.

The surface pressure characteristics on the OGVs are examined using the contours in Fig. 10 and 11. In both figures, the time-averaged surface pressure is $C_{p,\mathrm{mean}} = (\langle p \rangle - p_\infty)/(0.5\rho_\infty U_{\mathrm{ref}}^2)$, where $p_\infty = 101\,325\,\mathrm{Pa}$, while the RMS of surface pressure fluctuations is $C_{p,\mathrm{RMS}} = p_{\mathrm{RMS}}/(0.5\rho_\infty U_{\mathrm{ref}}^2)$.

In Fig. 10, the baseline OGV clearly shows a suction region near the LE (i.e., area with low $C_{p,\mathrm{mean}}$ at the suction side), particularly at the inner radius. These suction regions are no longer present in the M450 configuration. In the M450E case, the low-pressure regions are concentrated around the serration root, which compensates for the reduced aerodynamic loading at the serration tip; this can be clearly seen in plot (*a*) of Fig. 11. This plot also illustrates the separated-flow regions at the suction side of the M450 OGV, where the $C_{p,\mathrm{mean}}$ distribution downstream of the porous serrations ($x/c > 0.2$) is relatively flat. Differently, the pressure side of the M450 OGV exhibits a steeper slope compared to that of the baseline. This might be associated with the flow acceleration due to the narrower flow passage in the inter-OGV channel realised by the separated-flow region. For the M450E case, the plot in Fig. 11 (*b*) shows the pressure distribution on the porous segment of the serrations. The spatial distribution is similar as in plot (*a*), but the amplitude suction peak is less prominent due to the pressure balancing process in the porous medium region.

The lower half of Fig. 10 and 11 show the distribution of pressure fluctuations (in term of RMS values) on the OGVs. The contours in Fig. 10 show that the largest pressure fluctuations on the baseline OGV can be found near the outer span of the blades. On the M450 OGV, the pressure fluctuations are less intense. Nevertheless, Fig. 11 also evidences that $C_{p,\mathrm{RMS}}$ values on the M450 OGV tend to be higher than on the baseline blade near the trailing edge, especially at the suction side. This behavior is linked to the separated-flow region, which could induce a stall-noise mechanism [26] that enhances the broadband noise emission in the low-frequency range. For the M450E configuration, Fig. 10 also shows traces of strong pressure fluctuations downstream of the serration root. This phenomenon has been reported in literature [9, 27], which is caused by the reinforcement of upwash/downwash at the serration root due to the production of a secondary streamwise vortex system from the serration tip. The effect of permeability on the $C_{p,\mathrm{RMS}}$ level on the serrations can be observed by comparing the plots for the M450E configuration in Fig. 11 (*a*) and (*b*). At 90 % of outer radius, where the serrations are made of porous material, the peak $C_{p,\mathrm{RMS}}$ near the edge of the serration root is weaker than at 80 % of outer radius. Regardless, the usage of porous serrations at the outer span of the OGV in the M450E configuration can be considered beneficial since the overall $C_{p,\mathrm{RMS}}$ levels along the chord are lower

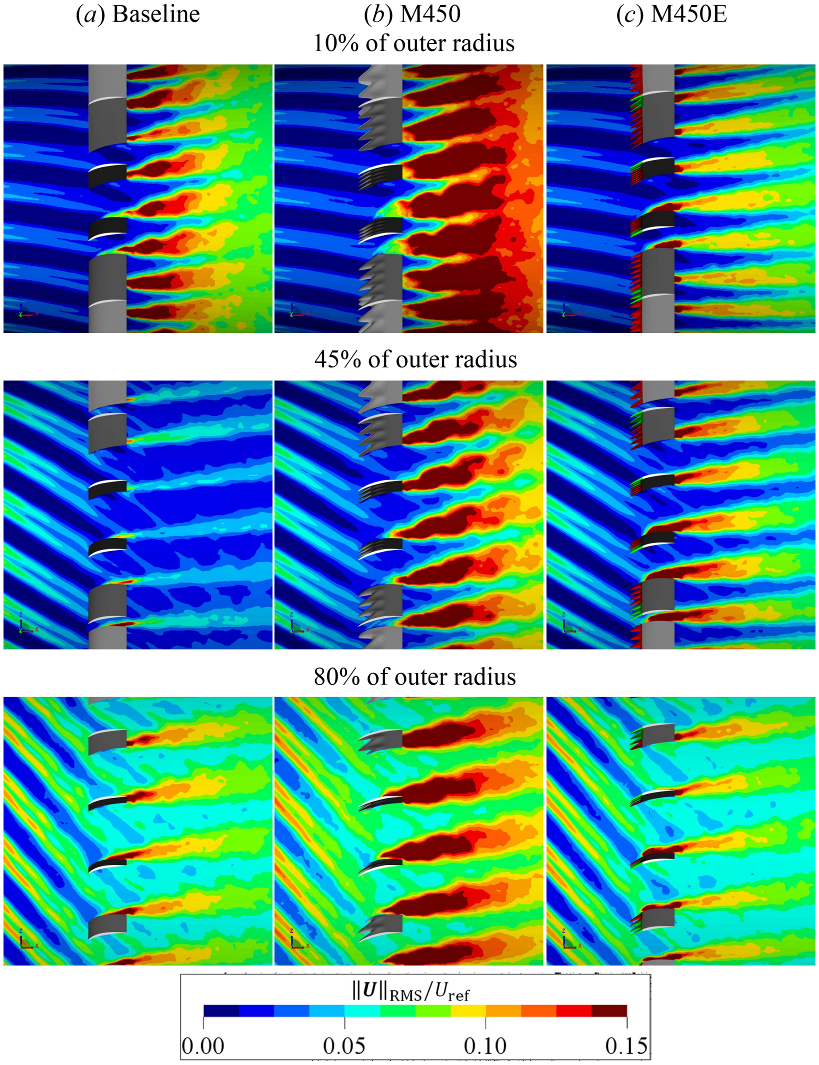

Fig. 9 (Side view) Contours of phase-locked standard deviation of velocity magnitude ($||U_{\mathrm{RMS}}||$) at the different radial sections (top - 10 %, middle - 45 %, and bottom - 80 % of the outer radius) in the fan stage.

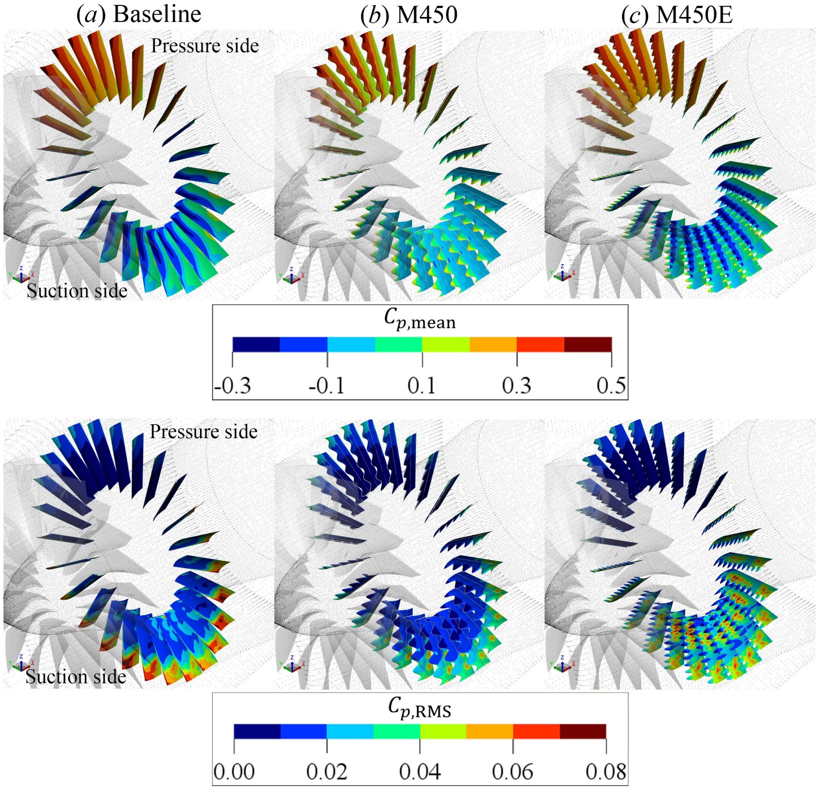

Fig. 10 (Isometric view) Contours of time-averaged surface pressure coefficient $C_{p,\text{mean}}$ and the RMS of surface pressure fluctuations $C_{p,\text{RMS}}$ on the OGV blades.

compared to the those in the baseline case.

C. Far-field noise characteristics

The dilatation field contour in Fig. 12 shows the acoustic field surrounding the aircraft model. The figure only shows the contour for the baseline configuration as it has been found that the contours for the other configurations are qualitatively similar. Sound waves that are generated by the fan-stage components can be seen to be radiated from the inlet and the outlet of the nacelle. The high-lift devices (e.g., slat and flap) located above the nacelle also diffract the impinging sound waves. The jet plume downstream of the nacelle also generates additional sound.

The effects of the OGV LE modification on the emitted acoustic power are examined in Fig. 13. The legend of plot (*a*) also lists the overall PWL (OPWL) values in the frequency range of $0.2 < f/\text{BPF}_1 < 3.5$. The plot clearly shows that only the M450E configuration achieves PWL reduction within the entire frequency range of interest. On the other hand, the M450 configuration exhibits enhanced broadband noise level in the low frequency range (i.e., $f/\text{BPF}_1 < 2$). As a consequence, the OPWL of the M450 configuration remains similar to that of the baseline despite the substantial reduction of the tonal noise component, as indicated in plot (*b*). The ΔOPWL bar chart also implies that the tonal noise reduction level is proportional to the extent of the porous serrations along the OGV span. The broadband noise increase in the M450 case might be associated with the severe flow separation that has been discussed in the previous subsection, which induces a stall-noise mechanism [26].

The noise directivity is depicted in term of the overall sound pressure level (OSPL) in Fig. 14. In the plot, OSPL values are reported at a distance of 120 m from the fan-stage inlet, which corresponds to the "approach" reference measurement distance [28] . Note that the aircraft nose is aligned with the 180° angle. The topmost plot shows that the sound is mainly radiated towards the downward direction, which can be attributed to the shielding effect due to the underwing placement of the fan stage [29]. The M450 configuration causes an OSPL increase of up to 2 dB relative to the baseline for most observation angles, except in the lower downstream direction (i.e., in between 310° and 330°). Conversely, no increase in OSPL can be found in the M450E case, and as such, the average OSPL reduction is 1 dB.

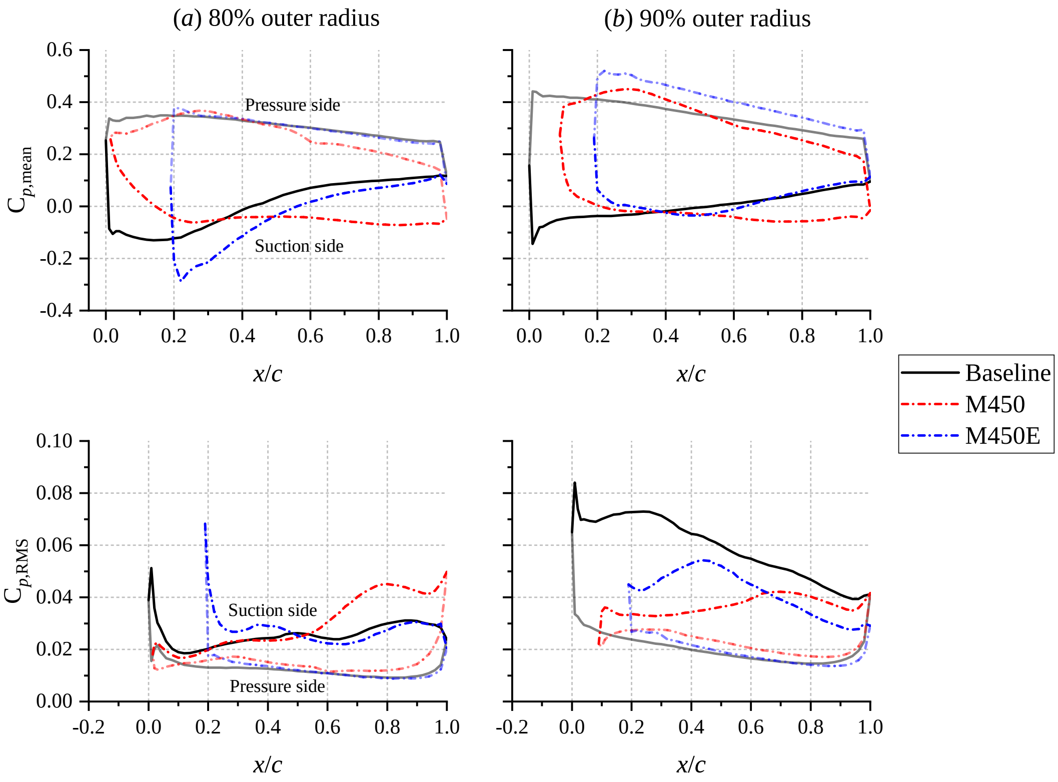

Fig. 11 Plots of (top row) time-averaged surface pressure coefficient and (bottom row) RMS of surface pressure fluctuations at the outer span of the OGV. Pressure coefficient values shown are averaged over the 26 blades. The pressure distributions at the pressure side are plotted with lower opacity. For the M450E configuration, note that the LE porosity is only implemented at > 85 % of the blade outer radius

.

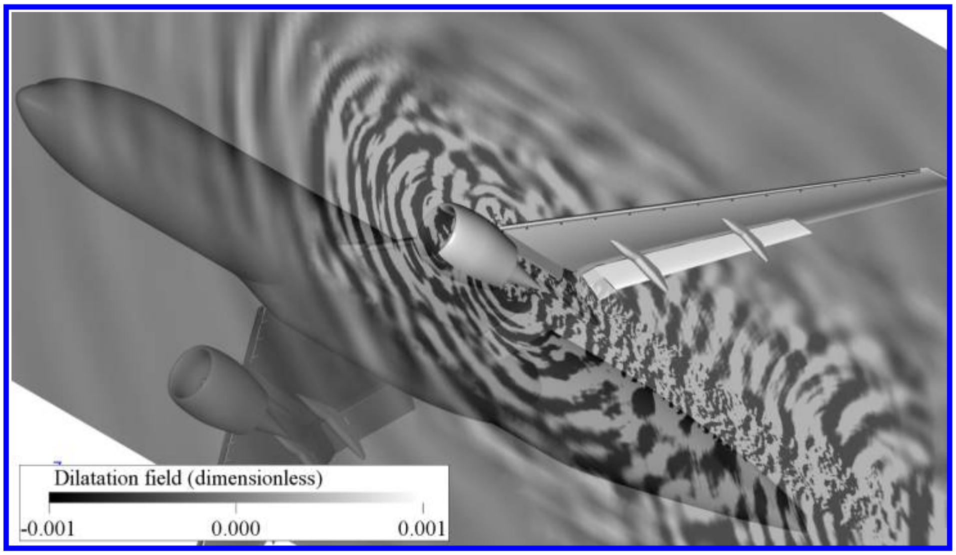

Fig. 12 The contour of the dilatation field (time derivative of pressure) surrounding the nacelle containing the SDT fan stage (baseline configuration). Note that the dilatation field is expressed in non-dimensional unit.

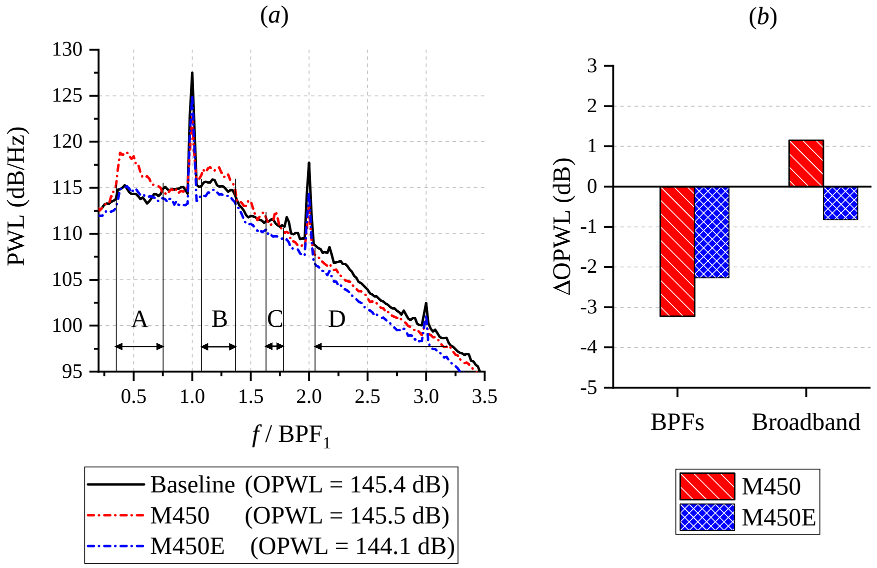

Fig. 13 (*a*) Source power level (PWL) of the CRM/SDT configuration. The capital letters denote the frequency ranges where the directivity patterns are plotted in Fig. 14. Plot (*b*) shows the OPWL difference between the modified configurations and the baseline, divided into two categories: BPFs (the tonal peaks BPF_1 to BPF_3) and broadband (the broadband noise component and other tones up to $f/\mathrm{BPF}_1 = 3.5$).

The lower half of Fig. 14 shows the directivity patterns at several frequency ranges that are highlighted in Fig. 13 (*a*). In the lowest frequency band ($0.35 < f/\mathrm{BPF}_1 < 0.75$), the M450 configuration exhibits a noise increase in all observation directions by up to 2.5 dB, while the OSPL of the M450E one is still comparable to the baseline case. The noise increase caused by the M450 configuration is also visible in plot B ($1.08 < f/\mathrm{BPF}_1 < 1.34$), although it becomes more directional towards the upper and lower directions. In plot C, the directivity pattern of the M450 configuration becomes more similar to the baseline one, whereas OSPL reduction towards the lower direction can already be observed in the M450E case. Plot D shows that high-frequency broadband noise reduction is present in both M450 and M450E configurations, although it is overall higher in the latter.

To demonstrate the relevance of the OGV LE modification on the noise level as perceived by ground observers, a noise footprint analysis is carried out *. For this purpose, the effective perceived noise level (EPNL) metric [28] has been employed to take into account the sensitivity of human hearing at different frequencies. In this analysis, the aircraft assumes an "approach" trajectory as illustrated in Fig. 15 (*a*). A reference downrange position has been selected where the aircraft altitude is 120 m. The aircraft has a descending flight path with a constant slope of 3 degrees, starting from a downrange coordinate 0.9 km to −0.9 km. The analysis also assumes the presence of a second engine underneath the starboard wing by mirroring the noise contribution from the SDT fan stage (which is installed underneath the port wing) along the symmetry plane of the aircraft. The noise footprint contours are plotted in Fig. 15 (*b*) and (*c*) over an area of $2.5 \times 2.5\,\mathrm{km}^2$. When compared to the baseline, the M450 configuration produces excess noise upstream of the aircraft while noise reduction is only present in the downstream direction, reflecting the sound directivity patterns in Fig. 14. On the other hand, the M450E configuration exhibits noise attenuation in the entire contour, although the EPNL reduction is generally higher behind the aircraft.

VI. Conclusions

This manuscript presents a numerical investigation on the application of a porous leading-edge (LE) treatment in a full-scale aircraft simulation. The aircraft model consists of the NASA HL-CRM airframe combined with the up-scaled NASA-SDT fan stage. To mitigate the fan wake-OGV interaction noise, the LE of the OGV is equipped with porous serrations that are modelled as a metal foam. This configuration is referred to as the M450 following the mean pore size of the metal foam, which is 450 µm. In one particular case (M450E), the usage of porosity is limited only at the outer

---

*This analysis has been performed using the *Opty∂B*-FOOTPRINT tool [30] in conjunction with 3DS-SIMULIA PowerACOUSTICS.

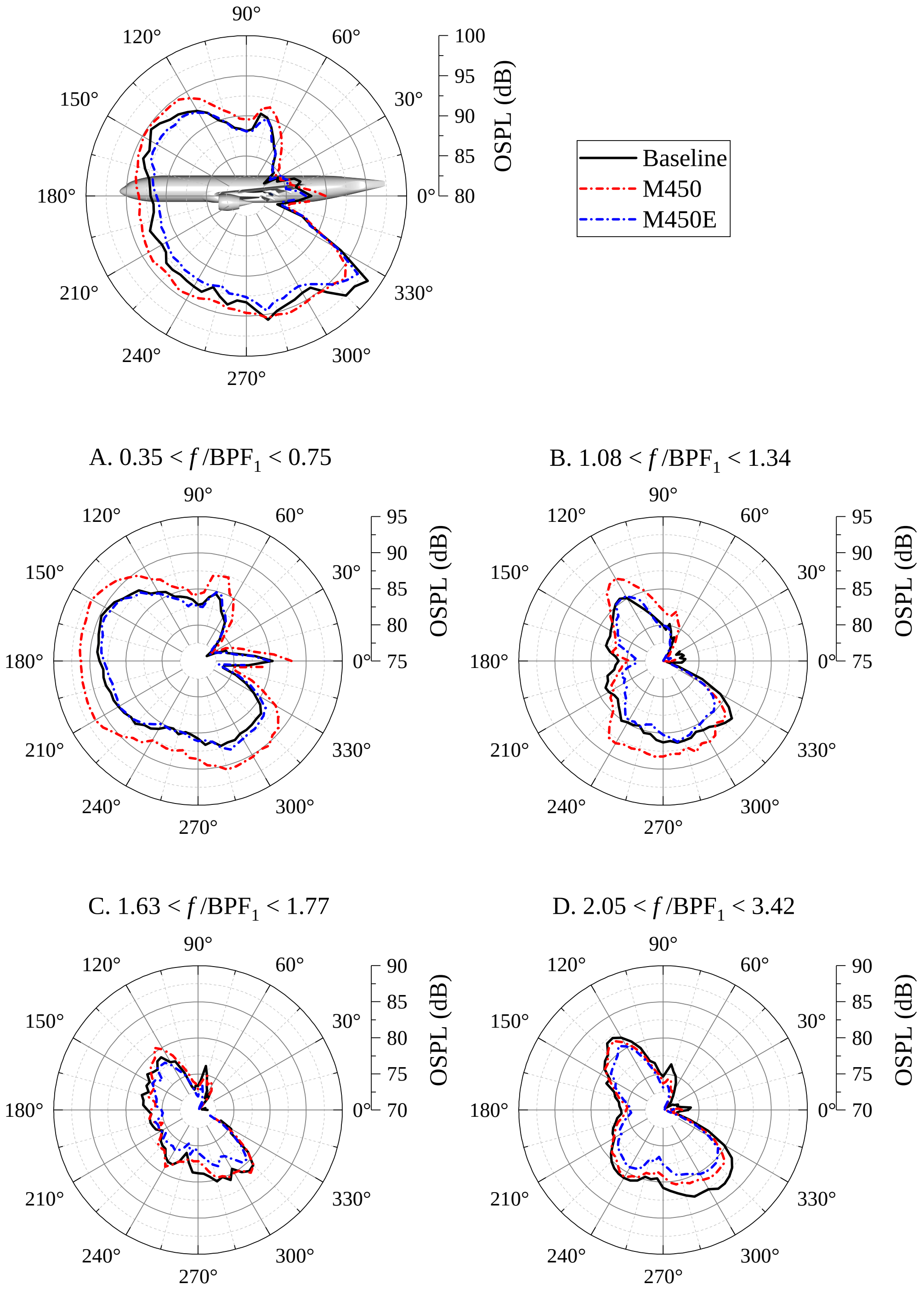

Fig. 14 The noise directivity pattern along the lateral axis. Directivity plots are also provided at frequency bands where notable discrepancies between the modified and baseline configurations are present in Fig. 13.

(*a*) Aircraft trajectory

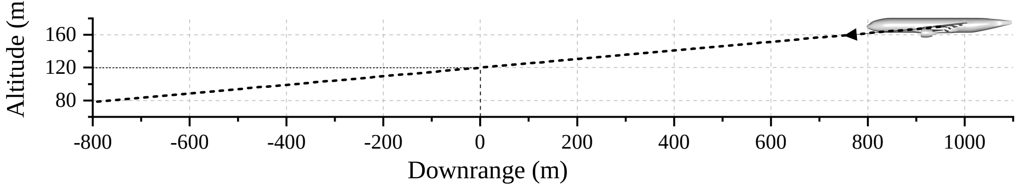

(*b*) Noise footprint during flyover

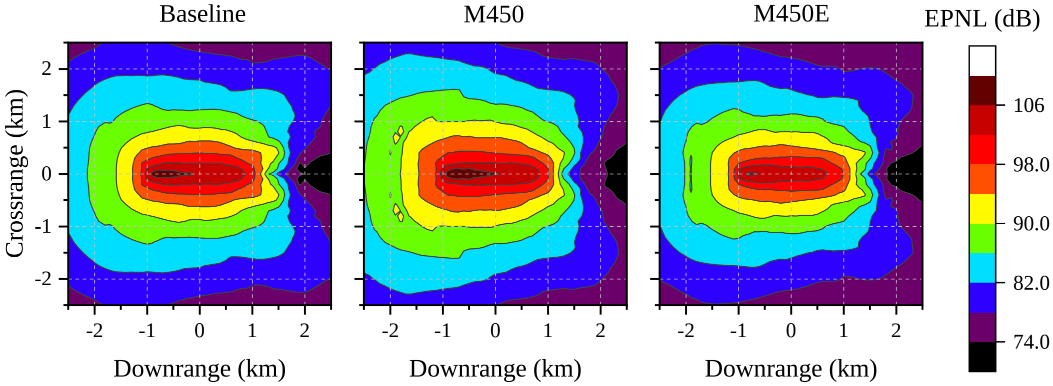

(*c*) EPNL difference

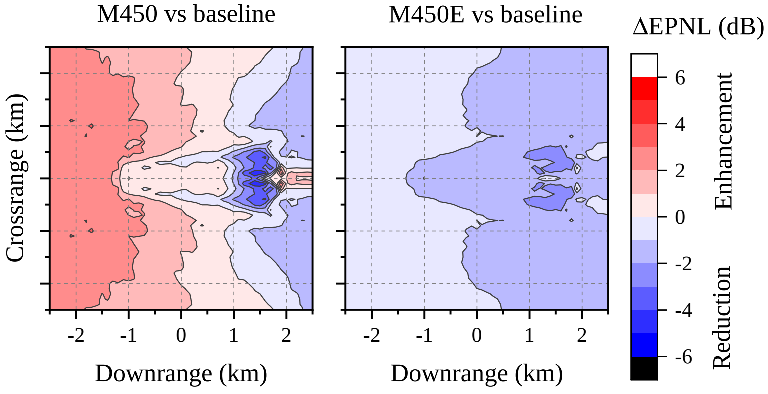

Fig. 15 (*a*) **The aircraft trajectory for noise footprint analysis,** (*b*) **noise footprint contours, in term of effective PNL (EPNL), corresponding to the aircraft trajectory.**

85 % of the OGV blade span, where the noise source intensity is expected to be the strongest.

The porous serrations yield a substantial tonal noise reduction at the blade-passage frequency (BPF) and its harmonics by up to 5 dB. However, the M450 configuration also exhibits an enhanced broadband noise level, especially in the low-frequency range. As a consequence, the overall source power level in the M450 case is relatively unchanged with respect to the baseline one, whereas a total of 1.5 dB reduction is achieved using the M450E configuration. Both noise directivity and noise footprint analyses reveal that the noise reduction is present mainly in the lower downstream direction. After examining the flow field in the fan stange, it is found that a severe flow separation at the suction side of the M450 OGV is responsible for enhancing the broadband noise emission. This process is induced by an unsteady cross-flow in the porous medium region due to the pressure imbalance between the suction and pressure sides of the OGV. The flow separation also decreases the mass flow rate in the fan stage, and in turn, the thrust output of the M450 case by more than 7 %. On the other hand, the thrust penalty in the M450E case is milder at 1.4 %. Thus, by limiting the implementation of porosity only at critical regions, it is possible to obtain a more favourable trade-off between acoustic and aerodynamic characteristics.

In summary, the present study has demonstrated the benefits from the application of porous serrations at the outer span of the OGV, which have been obtained for two reasons. Firstly, the fan wake impingement at these locations produces stronger unsteady loading on the OGV, and consequently, stronger noise sources, which can be suppressed more effectively using porous material. Secondly, the usage of porous material is less crucial at the inner radius of the fan stage, and thus, the inner span of the OGV is equipped with solid serrations to mitigate the adverse aerodynamic impact associated with a porous LE, such as the mean cross-flow between the suction and pressure sides of the blade.

Acknowledgments

The authors acknowledge the computing time on the Dutch National Computer Facilities, *Cartesius*, which has been provided by the Dutch Research Council (NWO) through the project 2021/ENW/01050159.

References

[1] Casalino, D., Diozzi, F., Sannino, R., and Paonessa, A., "Aircraft noise reduction technologies: a bibliographic review," *Aerospace Science and Technology*, Vol. 12, No. 1, 2008, pp. 1–17.

[2] Jacob, M. C., Boudet, J., Casalino, D., and Michard, M., "A Rod-Airfoil Experiment as a Benchmark for Broadband Noise Modeling," *Theoretical and Computational Fluid Dynamics*, Vol. 19, No. 3, 2005, pp. 171–196.

[3] Chen, W., Qiao, W., Tong, F., Wang, L., and Wang, X., "Numerical investigation of wavy leading edges on rod–airfoil interaction noise," *AIAA Journal*, Vol. 56, No. 7, 2018, pp. 2553–2567.

[4] Gea Aguilera, F., Gill, J. R., Angland, D., and Zhang, X., "Wavy leading edge airfoils interacting with anisotropic turbulence," *23rd AIAA/CEAS Aeroacoustics Conference*, 2017, p. 3370.

[5] Chaitanya, P., Joseph, P., Narayanan, S., Vanderwel, C., Turner, J., Kim, J.-W., and Ganapathisubramani, B., "Performance and mechanism of sinusoidal leading edge serrations for the reduction of turbulence–aerofoil interaction noise," *Journal of Fluid Mechanics*, Vol. 818, 2017, pp. 435–464.

[6] Roger, M., Schram, C., and De Santana, L., "Reduction of airfoil turbulence-impingement noise by means of leading-edge serrations and/or porous material," *19th AIAA/CEAS aeroacoustics conference*, 2013, p. 2108.

[7] Sarradj, E., and Geyer, T., "Noise generation by porous airfoils," *13th AIAA/CEAS Aeroacoustics Conference (28th AIAA Aeroacoustics Conference)*, 2007, p. 3719.

[8] Geyer, T. F., Lucius, A., Schrödter, M., Schneider, M., and Sarradj, E., "Reduction of turbulence interaction noise through airfoils with perforated leading edges," *Acta Acustica united with Acustica*, Vol. 105, No. 1, 2019, pp. 109–122.

[9] Teruna, C., Avallone, F., Casalino, D., and Ragni, D., "Numerical investigation of leading edge noise reduction on a rod-airfoil configuration using porous materials and serrations," *Journal of Sound and Vibration*, Vol. 494, 2021, p. 115880.

[10] Palleja-Cabre, S., Paruchuri, C. C., Joseph, P., Priddin, M. J., and Ayton, L. J., "Downstream Perforations for the Reduction of Turbulence-Aerofoil Interaction Noise: Part I-Experimental Investigation," *AIAA AVIATION 2021 FORUM*, 2021, p. 2149.

[11] Ayton, L. J., Colbrook, M. J., Geyer, T. F., Chaitanya, P., and Sarradj, E., "Reducing aerofoil–turbulence interaction noise through chordwise-varying porosity," *Journal of Fluid Mechanics*, Vol. 906, 2021.

[12] Lockard, D. P., Choudhari, M. M., O'Connell, M. D., Duda, B. M., and Fares, E., "Noise simulations of the high-lift common research model," *23rd AIAA/CEAS aeroacoustics conference*, 2017, p. 3362.

[13] Ribeiro, A. F., Ferris, R., and Khorrami, M. R., "Aeroacoustic Computations of a Generic Low Boom Concept in Landing Configuration: Part 2-Airframe Noise Simulations," *AIAA AVIATION 2021 FORUM*, 2021, p. 2196.

[14] Chen, H., Chen, S., and Matthaeus, W. H., "Recovery of the Navier-Stokes equations using a lattice-gas Boltzmann method," *Physical Review A*, Vol. 45, No. 8, 1992, p. R5339.

[15] Yakhot, V., and Orszag, S. A., "Renormalization group analysis of turbulence. I. Basic theory," *Journal of scientific computing*, Vol. 1, No. 1, 1986, pp. 3–51.

[16] Ffowcs-Williams, J., and Hawkings, D. L., "Sound generation by turbulence and surfaces in arbitrary motion," *Phil. Trans. R. Soc. Lond. A*, Vol. 264, No. 1151, 1969, pp. 321–342.

[17] Casalino, D., "An advanced time approach for acoustic analogy predictions," *Journal of Sound and Vibration*, Vol. 261, No. 4, 2003, pp. 583–612.

[18] Farassat, F., and Succi, G. P., "A review of propeller discrete frequency noise prediction technology with emphasis on two current methods for time domain calculations," *Journal of Sound and Vibration*, Vol. 71, No. 3, 1980, pp. 399–419.

[19] Sun, C., Pérot, F., Zhang, R., Lew, P.-T., Mann, A., Gupta, V., Freed, D. M., Staroselsky, I., and Chen, H., "Lattice Boltzmann formulation for flows with acoustic porous media," *Comptes Rendus Mécanique*, Vol. 343, No. 10-11, 2015, pp. 533–544.

[20] Woodward, R., Hughes, C., Jeracki, R., and Miller, C., "Fan Noise Source Diagnostic Test–Far-field Acoustic Results," *8th AIAA/CEAS Aeroacoustics Conference & Exhibit*, 2002, p. 2427.

[21] Rubio Carpio, A., Merino Martinez, R., Avallone, F., Ragni, D., Snellen, M., and van der Zwaag, S., "Broadband Trailing-Edge Noise Reduction Using Permeable Metal Foams," *INTER-NOISE and NOISE-CON Congress and Conference Proceedings*, Vol. 255, Institute of Noise Control Engineering, 2017, pp. 2755–2765.

[22] Casalino, D., Hazir, A., and Mann, A., "Turbofan broadband noise prediction using the Lattice Boltzmann Method," *AIAA Journal*, Vol. 56, No. 2, 2018, pp. 609–628.

[23] Podboy, G., Krupar, M., Helland, S., and Hughes, C., "Steady and unsteady flow field measurements within a NASA 22 inch fan model," *40th AIAA Aerospace Sciences Meeting & Exhibit*, 2002, p. 1033.

[24] Hansen, K. L., Kelso, R. M., and Dally, B. B., "Performance variations of leading-edge tubercles for distinct airfoil profiles," *AIAA journal*, Vol. 49, No. 1, 2011, pp. 185–194.

[25] Kim, J. W., Haeri, S., and Joseph, P. F., "On the reduction of aerofoil–turbulence interaction noise associated with wavy leading edges," *Journal of Fluid Mechanics*, Vol. 792, 2016, pp. 526–552.

[26] Brooks, T. F., Pope, D. S., and Marcolini, M. A., "Airfoil Self-Noise and Prediction," *NASA Reference Publication, NASA-RP-1218*, 1989.

[27] Turner, J. M., and Kim, J. W., "Aeroacoustic source mechanisms of a wavy leading edge undergoing vortical disturbances," *Journal of Fluid Mechanics*, Vol. 811, 2017, pp. 582–611.

[28] Boettcher, J., *Noise Certification Workshop*, 2006. URL `https://www.icao.int/Meetings/EnvironmentalWorkshops/Documents/Noise-Certification-Workshop-2006/Boettcher_3.pdf`.

[29] Bertsch, L., Heinze, W., Guérin, S., Lummer, M., and Delfs, J. W., "10 Years of Joint Research at DLR and TU Braunschweig toward Low-Noise Aircraft Design-What Did we Achieve?" *Aeronautics and Aerospace Open Access Journal*, Vol. 3, No. 2, 2019, pp. 89–105.

[30] Casalino, D., van der Velden, W. C., and Romani, G., "Community noise of urban air transportation vehicles," *AIAA Scitech 2019 Forum*, 2019, p. 1834.